Density currents front velocity uncertainty

Bruno Avila Farenzena [*], Jorge Hugo Silvestrini

Escola Politécnica, Pontifícia Universidade Católica do Rio Grande do Sul, Av. Ipiranga 6681, 90619-900 Porto Alegre - RS, Brazil

ARTICLE INFO

ABSTRACT

Lock-release density currents compose a family of stratified flows that consists of a rapid release of fluid initially confined in an environmental fluid, where the confined fluid usually has a higher density than the environment. When both fluids come into contact, a relative flow is initiated due to buoyancy force variation, configuring a density current. Density currents dynamics can be characterized by observing the temporal evolution of its frontal region position, and propagation velocity, usually referred to as front position and front velocity, respectively. The front position determination is associated with an arbitrary iso-value selection of a scalar field, for example, the density field. The front velocity is normally computed as its time derivative. Since the front position is measured in discrete data, local uncertainties are propagated to the front velocity, thus amplifying the error in its determination. Based in the planar lock-release setup and using numerical simulations as data acquisition method, this study proposes a new method of front position determination free of arbitrary iso-value choice and strategies to minimize local uncertainty errors in the temporal evolution of the front velocity. Obtained results show that the local uncertainty error in front velocity is a function of the spatial discretization, the temporal sampling and the numerical derivative method. Such error can be minimized by the use of interpolation in the front position acquisition method and/or using a new definition for the front velocity proposed in this study.

1. Introduction

Density currents (or gravity currents) compose a group of phenomena characterized by the relative flow between two fluids, with different densities, driven by buoyancy force variations. This phenomenon is widespread in nature, situations created by humans, and present in our daily lives where the density difference is, usually, caused by temperature, salinity, or humidity variations and/or particles in suspension [1]. In nature, for example, density currents can be observed in several cases, such as the formation of storms, caused by the relative displacement between large masses of hot air and masses of cold air; sandstorms, characteristic of sandy regions with low humidity, which transport large quantities of sand particles; and ocean currents that move due to the presence of gradients in saline concentration and water temperature [2].

The most straightforward approach to study density currents is the immediate release of a fixed volume of one fluid with a slightly higher density in a larger volume of a reference fluid initially separated by a lock gate. Such flow configuration is referred as lock-release density currents and can be employed to study density currents for different types of release, such as planar release [3–12], cylindrical release [5,13,14] and lock-basin release [15–19]. Fig. 1 depicts the initial configuration of this canonical set-up for a hyperpycnal planar release that was already investigated experimentally [3,4,6,8,10,11,13] and numerically [5,7,9,12], where the denser fluid is represented by the volume $L_{1,b}H \times H \times L_3 H$ and x_1 is the stream-wise direction, x_2 the vertical direction and x_3 the span-wise direction.

Many authors have described the dynamics of a density current based on the temporal evolution of the frontal region position and velocity [13,20,21]. Taking as example a planar release, after a rapid acceleration promoted by the initial condition in the initial time, a lock-release density current has three flow phases related to the behavior of the front velocity. Firstly the flow experiments a state referred to as the slumping phase. The current is retarded by the counter-flow associated with the environmental fluid, resulting in a period where the flow propagates with nearly constant velocity. This period is followed by a inertial state, where the inertial forces of the current balance the buoyancy force of the intruding fluid. Such an inertial phase is characterized by the density current front velocity decaying proportionally to $t^{-1/3}$ [13,20]. Finally, when the inertial effects become negligible, the buoyancy force is balanced by the viscous forces initiating the viscous phase, in which the rate of advancement of the current is proportional to $t^{-5/8}$ [20]. Based on these previous observations, the proper quantification of the front velocity becomes an essential key point in understanding the dynamics of density currents.

---

* Corresponding author.
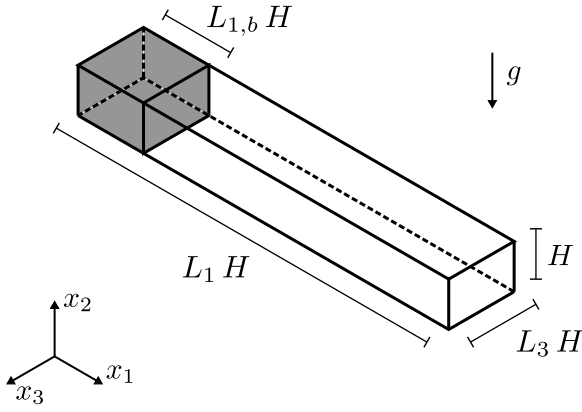*E-mail address:* Bruno.Farenzena@edu.pucrs.br (B.A. Farenzena).

Fig. 1. Schematic view of the initial configuration of a lock-release gravity current for a planar release.

The density current front velocity is naturally defined as the time derivative of the front position [5]. In numerical and experimental approaches, the front velocity is measured from discrete data with uncertainties associated with the resolution of the data acquisition method. Such uncertainties are propagated and amplified to the front velocity, resulting in noisy signals that do not allow the definition of the front velocity for a given time. In this context, the present study has the main objective of quantify these local uncertainties and propose strategies and methods to minimize them. To do it so, firstly, we understand the origin of uncertainties and which parameters governs their propagation and amplification using numerical simulations of lock-release hyperpycnal density currents in the planar release configuration as data acquisition method. After we propose guidelines to minimize the local uncertainties and a new definition to quantify front velocity based in a moving frame approach.

This paper is organized as follows: firstly, in Section 2, we describe the mathematical model and the computational code employed to perform the numerical simulations; in Section 3 we introduce the method considered to measure the front position from data; Section 4 shows the front velocity definition and its local uncertainties; during Section 5, different strategies to minimize the local uncertainties are proposed; the results including the local uncertainties quantification, the sensibility of the front velocity to the different proposed strategies and comparison with results of [5] are presented in Section 6; and finally, in Section 7, we present the summary of all observations and the conclusions.

2. Numerical simulations formulation

To mathematically describe the lock-release density current in the planar release configuration presented in Fig. 1, we need to define governing equations, boundary conditions, and an initial condition. This flow configuration is assumed to be an incompressible flow in which the Boussinesq approximation can be employed. Under such a hypothesis, the flow is described by a system of partial differential equations composed by the Navier–Stokes equations for Newtonian fluids and a scalar transport equation for the density fluctuation field. The governing equations are given in the dimensionless form:

$$\boldsymbol{\nabla} \cdot \boldsymbol{u} = 0, \tag{1}$$

$$\frac{\partial \boldsymbol{u}}{\partial t} + (\boldsymbol{u} \cdot \boldsymbol{\nabla}) \, \boldsymbol{u} = -\boldsymbol{\nabla} p + \frac{1}{Re} \boldsymbol{\nabla}^2 \boldsymbol{u} - \varphi e_2, \tag{2}$$

$$\frac{\partial \varphi}{\partial t} + (\boldsymbol{u} \cdot \boldsymbol{\nabla}) \, \varphi = \frac{1}{ScRe} \boldsymbol{\nabla}^2 \varphi, \tag{3}$$

being $\boldsymbol{x} = (x_1, x_2, x_3)$ the coordinate system, t the time, $\boldsymbol{u} = (u_1, u_2, u_3)$ the velocity field, p the pressure, φ the density fluctuation, e_2 the unitary vector oriented in the vertical direction, Re the Reynolds number

and Sc the Schmidt number. The dimensionless density fluctuation is related with the fluid density by the equation:

$$\rho = \Delta\rho \, \varphi + \rho_0, \tag{4}$$

being $\Delta\rho$ the density difference between both fluids and ρ_0 the light fluid density.

The presented mathematical model is made dimensionless using the buoyancy velocity as velocity scale and the heavier fluid column height H as length scale. Such a velocity scale is based on an inviscid energy budget that considers a full-transformation of the initial potential energy into kinetic energy [2]. The result of this energy budget is a flow velocity, usually referred to as buoyancy velocity, defined as

$$u_b = \sqrt{\frac{\Delta\rho}{\rho_0} g H} \tag{5}$$

where g is the gravity acceleration. Using these characteristic length and velocity values, the (bulk) Reynolds number is defined as

$$Re = \frac{H u_b}{\nu} = \frac{H}{\nu} \sqrt{\frac{\Delta\rho}{\rho_0} g H}, \tag{6}$$

where ν the reference fluid kinematic viscosity. It is noteworthy that the Richardson number is not explicit as a free parameter due to the convenient choice of characteristic scales. The Schmidt number is defined as the ratio between the fluid kinematic viscosity and the suspension mass diffusivity, which value is assumed equals to 1 in this work. Finally, the resulting geometrical domain after normalizing by the length scale is $L_1 \times 1 \times L_3$.

The boundary conditions considered are for the velocity: no-slip in $x_2 = 0$ and free-slip in $x_1 = 0$, $x_1 = L_1$ and $x_2 = 1$; and for the scalar field no scalar flux in $x_1 = 0$, $x_1 = L_1$, $x_2 = 0$ and $x_2 = 1$; periodicity is imposed in the x_3 direction for both scalar and velocity fields. The initial condition of the scalar field is prescribed with the use of a smooth function in order to avoid local discontinuities

$$\varphi(\boldsymbol{x}, t = 0) = \frac{1}{2} - \frac{1}{2} \tanh \left[\delta \left(x_1 - L_{1,b} \right) \right]. \tag{7}$$

with $\delta = \sqrt{ReSc}$ [7]. A weak random number perturbation is superposed in all velocity components positioned at (the lock position) $x_1 = L_{1,b}$.

The numerical simulations are carried out with the high-order finite differences parallel open-source code Xcompact3D [22]. The code is based on sixth-order compact schemes for spatial discretization [23], and a third-order explicit Adams–Bashforth method for time integration. The momentum equation's non-linear term is computed in the skew-symmetric form to reduce aliasing and to increased stability [24]. In contrast, the transport equation non-linear term is computed in the divergence form due to non-homogeneous boundary conditions. The pressure gradient is obtained via a fractional step (prediction/correction method) by solving a Poisson equation in the spectral space with a distributed Fast Fourier Transform (FFT) package.

Three numerical simulations were performed varying the Reynolds number with fixed domain size, as summarized in Table 1. The Reynolds numbers chosen are the same as in Ref. [5], and the domain size is equivalent to the "small release" setting of the same work. The "small release" setting from [5] consists in Direct Numerical Simulations (DNS) of planar lock-release gravity currents with $L_{1,b} = 1$ and Reynolds number 895, 3450 and 8950 and, among other results, the authors provides both front position and velocity. Additionally to the numerical results from [5] we compare our results with experimental data from [4], specially the "Run 3" that has mostly the same setting with a slightly smaller Reynolds number, which is 8620.

For $Re = 895$ and $Re = 3450$ we solve the mathematical problem using the DNS approach while the $Re = 8950$ case is solved with Implicit Large Eddy Simulation (ILES) approach, proposed by [25]. The Implicit Large Eddy Simulation approach employed in this work is based on an artificial dissipation added to the second derivative

Table 1
Numerical simulations parameters. All simulation with $L_1 = 16$, $L_{1,b} = 1$, $L_3 = 1$ and $Sc = 1$.

Simulation	Re	$n_1 \times n_2 \times n_3$	Δt	t_f	Approach
Re895	895	$1281 \times 81 \times 80$	5×10^{-4}	70	DNS
Re3450	3450	$2561 \times 161 \times 160$	5×10^{-4}	50	DNS
Re8950	8950	$1601 \times 101 \times 100$	8×10^{-4}	45	ILES

numerical scheme, mimicking a spectral vanishing viscosity model behavior [25]. As described by [25], this alternative approach allows us to perform cheaper numerical simulations with no need of explicit sub-grid models. A recent investigation of ILES approach employment to simulate lock-release gravity currents has been performed by [12], where the authors compared the results with DNS (validated with experimental data) and classical (explicit) Large Eddy Simulation (LES) approaches. It was found that the ILES approach can reproduce the main features and global quantities of a lock-release gravity current, with approximately 0.4% of the grid points used in the DNS and slightly more accurate results than the classical LES approaches. Since the present study is concerned with measuring global quantities of lock-release gravity current, the ILES approach is considered appropriate. More information about the criteria employed to choose the number of grid points for each simulation case can be found in Appendix.

3. Front position

We consider the concept of layer-averaged thickness, denoted as h_{LA}, proposed by [26] to evaluate the front position of the gravity current. Such quantity is a function of the stream-wise coordinate (x_1) and time (t) being defined as:

$$h_{LA}(x_1, t) = \frac{(UL)^2}{U^2 L}, \tag{8}$$

with

$$UL(x_1, t) = \frac{1}{L_3} \int_0^{L_3} \int_0^h u_1(\boldsymbol{x}, t) dx_2 dx_3 \tag{9}$$

$$U^2 L(x_1, t) = \frac{1}{L_3} \int_0^{L_3} \int_0^h \left[u_1(\boldsymbol{x}, t) \right]^2 dx_2 dx_3, \tag{10}$$

where h is the distance from the bottom of the channel to the interface between the gravity current and the ambient fluid, which is a function of $\boldsymbol{x}$ and t. Additionally, we compute an interface where the stream-wise velocity component is zero, meaning that the layer-averaged thickness only accounts for the current motion in a single direction (from $x_1 = L_{1,b}$ towards $x_1 = L_1$). The layer-averaged thickness estimation is performed with the aid of a simple mask function (f_{mask}) defined as

$$f_{mask} = \begin{cases} 1, & u_1(\boldsymbol{x}, t) > 0 \\ 0, & otherwise \end{cases}. \tag{11}$$

Finally, the UL and $U^2 L$ quantities are evaluated as

$$UL(x_1, t) = \frac{1}{L_3} \int_0^{L_3} \int_0^1 f_{mask} u_1(\boldsymbol{x}, t) dx_2 dx_3 \tag{12}$$

$$U^2 L(x_1, t) = \frac{1}{L_3} \int_0^{L_3} \int_0^1 f_{mask} \left[u_1(\mathbf{x}, t) \right]^2 dx_2 dx_3, \tag{13}$$

Fig. 2 depicts the concept for the gravity current front position measurement ($x_{f,m}$) and its relation with the span-wise averaged density field, using results from the simulation Re3450 for $t = 15$. For each snapshot, farthest local minimum of h_{LA} (evaluating from the lock-gate towards the end of the channel) expresses the front position.

The presented method of front position determination has an advantage compared with traditional methods for being parameter-free as no threshold of density fluctuation has to be specified, relying on a local minimum of a integral quantity.
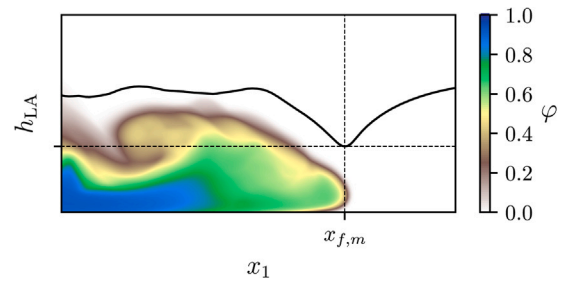

Fig. 2. Example of the density current front position measurement based on the first local minimum of h_{LA} and its relation with the span-wise averaged density field. This figure is rendered using results from the simulation Re3450 for $t = 15$.
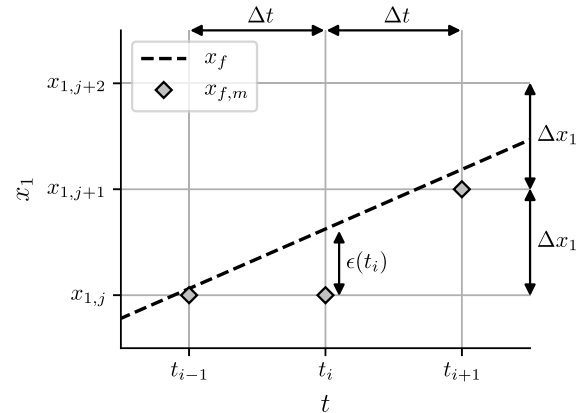

Fig. 3. Scheme of the uncertainty associated with the front position measured in a discrete mesh.

4. Front velocity and its local uncertainties

The front velocity of a density current (u_f) for any given time is defined as the time derivative of the front position (x_f), in the form:

$$u_f(t) = \frac{dx_f}{dt}. \tag{14}$$

Since the front position is measured from discrete data, the evaluation of the front velocity is performed with a measured front position ($x_{f,m}$), that have the form:

$$x_f(t) = x_{f,m}(t) + \epsilon(t), \tag{15}$$

being ϵ the measurement error. The value of such an error is not known. However, it can vary in the interval $0 < \epsilon(t) < \Delta x_1$, and can be easily understood with the aid of Fig. 3 by supposing the existence of a continuous front position signal and a measured signal bounded to a spatial discretization with resolution Δx_1.

Taking as reference the central second-order finite difference scheme, we estimate the front velocity for a time instant t_i in the form:

$$u_f(t_i) = \frac{dx_f}{dt}\bigg|_{t_i} = \frac{x_f(t_{i+1}) - x_f(t_{i-1})}{2\Delta t} + O(\Delta t^2), \tag{16}$$

where Δt is the temporal sampling $O(\Delta t^2)$ is the finite difference scheme's truncation error. By introducing the measured front position concept, described by Eq. (15), in the front velocity approximation, it is possible to identify another source error associated with the uncertainty

of the front position measurement, denoted as $\mathcal{E}$:

$$
\begin{aligned}
\left.\frac{dx_f}{dt}\right|_{t_i} = {} & \frac{x_{f,m}(t_{i+1}) - x_{f,m}(t_{i-1})}{2\Delta t} \\
& + \underbrace{\frac{\epsilon(t_{i+1}) - \epsilon(t_{i-1})}{2\Delta t}}_{\mathcal{E}} + O(\Delta t^2).
\end{aligned}
\tag{17}
$$

Using the definition of the front position measurement uncertainty, we estimate the local uncertainty error $\mathcal{E}$ as:

$$
\mathcal{E} = \frac{\epsilon(t_{i+1}) - \epsilon(t_{i-1})}{2\Delta t} = \pm O\left(\frac{\Delta x_1}{2\Delta t}\right).
\tag{18}
$$

When the same analysis is performed for other finite difference schemes, for example, the first order and central fourth order schemes, the local uncertainty error is estimated, respectively, in the form:

$$
\mathcal{E} = \pm O\left(\frac{\Delta x_1}{\Delta t}\right),
\tag{19}
$$

$$
\mathcal{E} = \pm O\left(\frac{9}{12}\frac{\Delta x_1}{\Delta t}\right),
\tag{20}
$$

Such simple analysis shows that the local uncertainty error is a function of the front position measurement resolution, the temporal sampling, and the numerical scheme employed to estimate the front velocity. Since the higher-order schemes tend to amplify even more the local uncertainty error, as observed when Eqs. (18) and (20) are compared, we restrain our analysis of this error in the numerical simulations to the central second-order finite difference scheme.

We expect the ILES to have a larger local uncertainty error than DNS for a given Reynolds number because an ILES, typically, employs coarser meshes [12,25]. For example, in the simulation Re8950, it is estimated that the ILES have a local uncertainty error of approximately 6 times greater than its equivalent DNS. This estimation assumes that an ILES requires approximately 0.4% grid points of a DNS [12] and that the same temporal sampling is considered for both approaches. Such estimation reinforces the importance of reducing the local uncertainty error when determining the front velocity, especially for the ILES approach.

5. Reducing local uncertainty error

This section addresses to the description of two different approaches to minimize the local uncertainty errors previously. Firstly we present one approach based on measuring the front position more precisely with the aid of cubic spline interpolation [27], thus reducing the ϵ value in Eq. (17). Afterwards, we introduce a new definition of the front velocity, based in a moving frame approach, free of the local uncertainty error previously defined.

5.1. Refined front position measurement

This approach aims to refining the front position measurement based on the minimum of Eq. (8), resulting in a refined front position, denoted as $x'_{f,m}$, for any given time. It is accomplished by performing a cubic spline interpolation in the layer-averaged thickness h_{LA} for the initially measured front position vicinity. Assuming that the cubic spline provides a better measurement of the desired local minimum of h_{LA}, the refined front position value is obtained by finding the minimum associated with the cubic spline interpolation, as shown in Fig. 4. Since the difference between the initial and the refined front position measurements is always bounded to the $0 \leq x_1 - x_{f,m} < \Delta x_1$ range, such an assumption is a reasonable one to minimize the error between the actual front position and the measured one, as previously described in Fig. 3. On the other hand, even this slight difference in the front position significantly impacts the front velocity when is evaluated because the local uncertainty error $\mathcal{E}$ is reduced (Eq. (18)).

It is important to note that the same approach can be adapted to refine the front position measurement of the φ projections method proposed in [5], but it will not be explored in the present work.
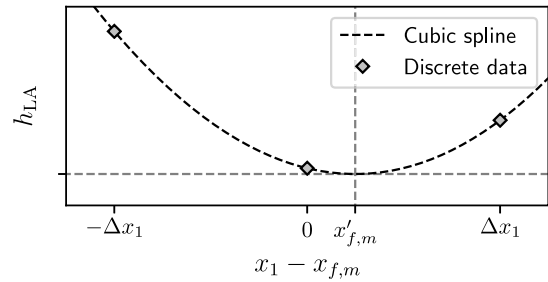

Fig. 4. Example of the front position refined measurement ($x'_{f,m}$) with the aid of the cubic spline interpolation associated with the layer-averaged thickness h_{LA} of the discrete data for a given time.

5.2. The moving frame method

This new approach targets the front velocity determination using a new definition, different from Eq. (14), based on the assumption of the existence of a hypothetical moving frame, with constant velocity and oriented in the stream-wise direction, that keeps the front position in equilibrium for a given time. It is achieved by approximating the scalar temporal variation in the form:

$$
\frac{\partial \varphi}{\partial t} \approx -u_{f,\mathrm{MF}}\frac{\partial \varphi}{\partial x_1},
\tag{21}
$$

being $u_{f,\mathrm{MF}}$ the moving frame constant velocity. By substituting the Eq. (21) in Eq. (3) and integrating in the vertical and span-wise directions, we find a relation to calculate the moving frame velocity:

$$
u_{f,\mathrm{MF}} = \frac{\displaystyle\int_0^{L_3}\int_0^1 \left(u_1\varphi - \frac{1}{ReSc}\frac{\partial \varphi}{\partial x_1}\right)dx_2 dx_3}{\displaystyle\int_0^{L_3}\int_0^1 \varphi\, dx_2 dx_3}.
\tag{22}
$$

When Eq. (22) is evaluated in the measured front position ($x_1 = x_{f,m}$), it provides the front velocity.

6. Results

The results presentation is divided into three parts: initially, the general features of a lock-release gravity current are presented with instantaneous flow visualizations. Afterward, we show the front position obtained using the previously presented approaches. Finally, we present the front velocity evaluation and its uncertainty.

In Fig. 5 is presented the temporal evolution of the planar gravity current using volume rendering visualizations for the scalar field φ of the case Re8950 for $t = 0$ (a), $t = 10$ (b) and $t = 15$ (c). As the current propagates towards the end of the channel, it spreads along the bottom plane ($x_2 = 0$). We can observe the formation of Kelvin–Helmholtz billows behind the head and its propagation towards the back, and also the formation of lobe and cleft structures characterized by the heterogeneity in the current frontal region [3,5]. As time goes on, the gravity current is mixing and entraining the ambient fluid due, mainly, to both Kelvin–Helmholtz billows and lobe and cleft structures. This dissipative process is qualitatively indicated by the decreasing of the scalar field φ amplitude, which the mean value varies from 1 ($t = 0$) to approximately 0.6 ($t = 15$), and for a sufficient long time instant ($t \to \infty$, for example) this mean value is approximately $L_{1,b}/L_1$ [28]. The formation of such coherent structures in hyperpycnal density currents are described and well reported in the literature [2,29] as predominant flow features. Moreover, its reproduction suggests that the performed numerical simulations are qualitatively suited to analyze this flow type, even using the Implicit Large Eddy Simulation approach (Fig. 5).

The front position for each case is presented in Fig. 6, where is adopted the refined front position measurement ($x'_{f,m}$) to compare with
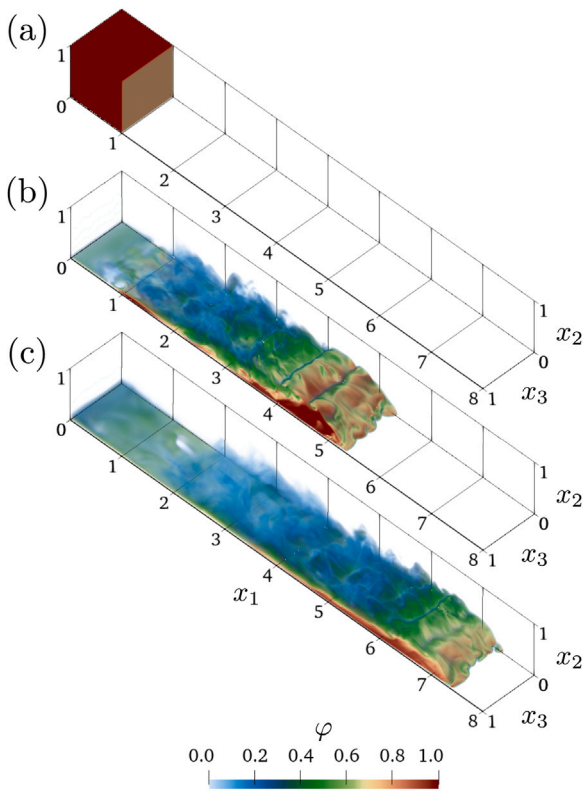
Fig. 5. Volume rendering of the density fluctuation field of the case Re8950 for the time instants $t = 0$ (a), $t = 10$ (b) and $t = 15$ (c).

results from [4,5]. As expected in the literature, after a brief moment of acceleration, the flow propagates with constant velocity for a time period, which goes until $t \approx 12$ in the simulation cases. Such a period is referred to as the slumping phase and can be noted by the front position linear behavior in Fig. 6. With the time increment, the flow experiments a transition towards the inertial phase and after the viscous phase, and the front positions have no longer a linear behavior. The transition to the inertial and viscous phases will be further explored with the front velocity due to its simplicity. It is also noted that the higher Reynolds number values are considered, the faster the density current propagates, as the flow needs a smaller period to reach the end of the channel ($x_1 - L_{1,b} = 15$). In general, the front position measured in the simulations has a good agreement with the data available in the literature. It presents small deviations mainly when $t > 15$, which are attributed to the proposed front position measurement method. However, even with these small deviations from the reference data, the front position expected behavior along the time is reproduced.

Considering the second-order central finite difference scheme and time sampling $\Delta t = 0.1$, the front velocity based on the time derivative of the front position measurement is evaluated as a function of the time for each simulation case, presented in Fig. 7. The resulting signal is noisy and difficult to analyze. However, it has the main expected features, such as the rapid acceleration during initial time instants followed by a period with nearly constant velocity and, finally, the decaying velocity period (Fig. 7a). Unfortunately, the decaying slope corresponding to the inertial or viscous phases [13,20] is not observed due to the noise. The local uncertainty error causes this noise in the signal, characterized by the front velocity jumps easily observed in Fig. 7b. The amplitude of these jumps is measured as 6.25×10^{-2}, 3.125×10^{-2} and 5×10^{-2} for the cases Re895, Re3450 and Re8950 respectively, which is equal to the estimation provided by Eq. (18) for each simulation. The agreement between the local uncertainty amplitude measured in the signal and the estimations provided by Eq. (18), confirms that the

source of this noise is the combination of the numerical derivation method with the front position measurement bound to discrete data, as stated before.

To reduce the local uncertainty error in the front velocity, we employ both previously described methods. Firstly, we consider the time derivative of the refined front position measurement for each case, with the second-order central finite difference scheme and a time sampling $\Delta t = 0.1$, which results are shown in Fig. 8. Afterward, we evaluate the front velocity using the moving frame method for each simulation, as presented in Fig. 9. In both figures, the decaying slopes $t^{-1/3}$ (dashed line) and $t^{-5/8}$ (dash-dotted line) corresponds to the inertial and viscous phases respectively [13,20].

Using the refined front position measurement to determine the front velocity (Fig. 8), we clearly note a drastic reduction in the signal noise when compared with Fig. 7a. For the simulation cases Re895 and Re3450, the noise is mostly damped. In contrast, the case Re8950 still has a residual noise but with a smaller amplitude, which can be attributed to the coarse mesh employed in the Implicit Large Eddy Simulation approach. The characteristics decaying slopes that occur after the slumping phase can be identified, where the viscous phase is predominant for the cases Re895 and Re3450, which is expected due to its lower Reynolds number [5]. For $Re = 8950$, the flow experiments a brief time period in the inertial phase, and then it transitions to the viscous phase.

When the front velocity based on the moving frame method is considered (Fig. 9) it results in a smooth signal for all simulation cases with the characteristics previously described, with major differences for $t \leq 1$ when compared with Figs. 7a and 8. Such differences in the acceleration phase can be negligible because, after this short period, the simulations reaches the expected self-similar states [13,20].

Taking the front velocity based on the moving frame method as reference, the entire time series is compared with the numerical results from [5] and the experimental results from [4] as presented in Figs. 10a, 10b and 10c. During the acceleration phase, our results estimate a maximum front velocity 14% greater than the results from [5], on average. Except this difference, there is good agreement with the literature results for the rest of the time series. When compared with the experimental results in Fig. 10c our numerical results tend to underestimate the front velocity by 9% on average, which is the same tendency observed in [5]. Such difference in the front velocity between numerical and experimental approach can be attributed to the different initial conditions and Schmidt number. In numerical studies it is often employed $Sc = 1$ for computational reasons and the experiments from [4] have $Sc \approx 700$.

Considering both the time derivative of the refined front position measurement and the moving frame method, we determine the time-averaged front velocity during the slumping phase $u_{f,s}$ and compare with results from [5], as presented in Fig. 10d. This time-averaged quantity is determined as

$$u_{f,s} = \frac{1}{t_{s,f} - t_{s,0}} \int_{t_{s,0}}^{t_{s,f}} u_f \, dt, \tag{23}$$

being $t_{s,0}$ and $t_{s,f}$ the initial and final times of the slumping phase respectively, which we consider $t_{s,0} = 2.5$ and $t_{s,f} = 10$ for all simulation cases. As previously mentioned, the higher is the Reynolds number, the greater is the front velocity and this quantity present an asymptotic value of 0.5 when $Re \to \infty$ [5]. Compared with the data available in the literature, our results present a maximum relative difference of approximately $3,5\%$. Simultaneously, the comparison between both front velocity determination methods shows a small difference, estimated at approximately 0.2%.

7. Summary and conclusions

Motivated by the reproduction of the self-similar flow phases of lock-release density currents [13,20], the uncertainty associated with
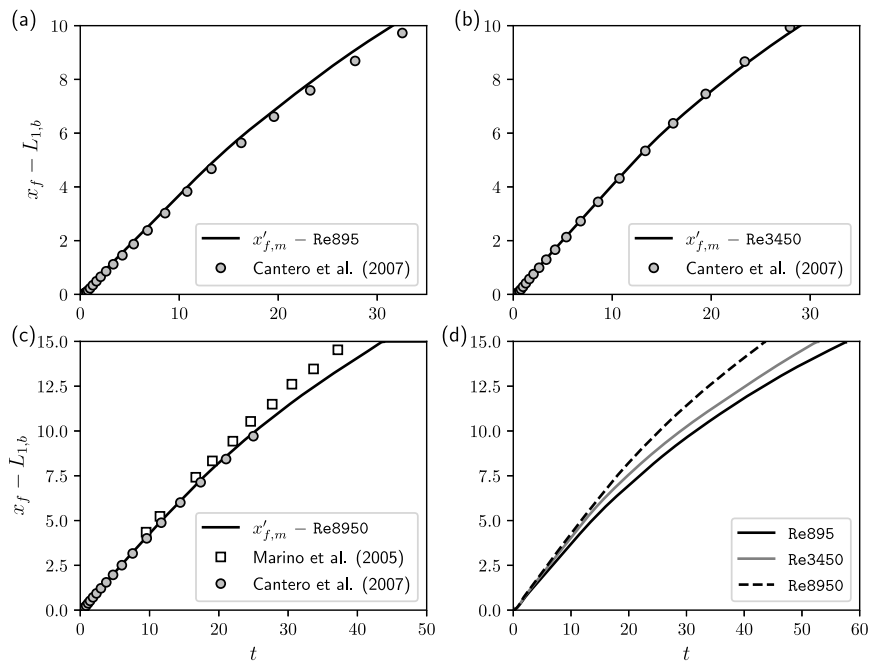
Fig. 6. Front position as function of time. Comparison with results of [4,5] for the cases Re895 (a), Re3450 (b) and Re8950 (c), while (d) presents all cases.
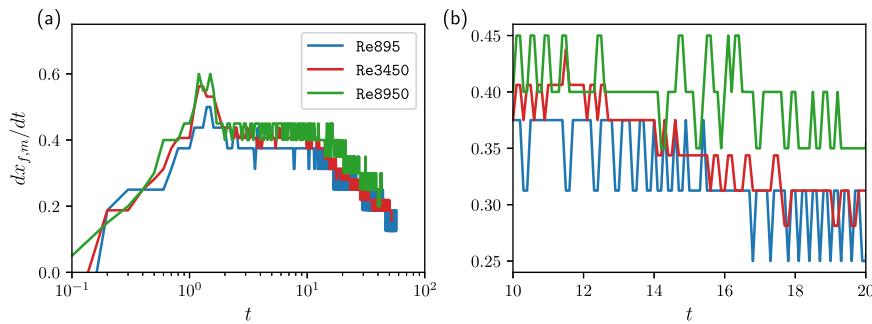

Fig. 7. Front velocity based on the time derivative of the front position measurement as function of time, where (a) presents the results for the complete simulation time span and (b) shows the results for time interval $10 \leq t \leq 20$.
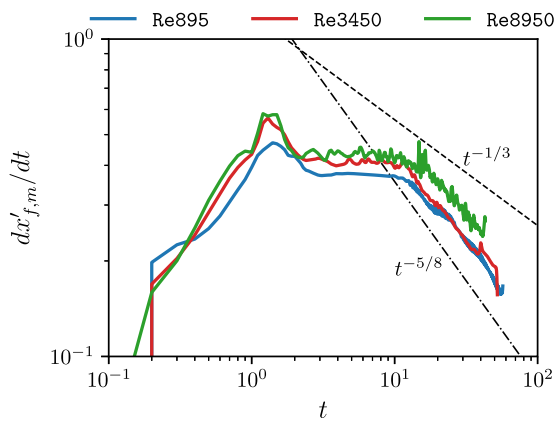

Fig. 8. Front velocity based on the time derivative of the refined front position measurement as function of time.
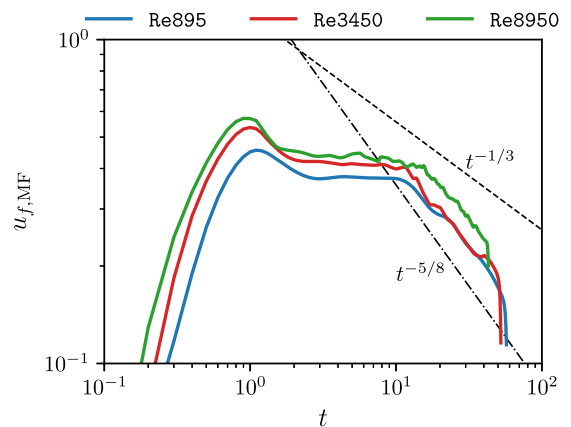

Fig. 9. Front velocity based on the moving frame method as function of time.

the front velocity determination was investigated in this paper. Such uncertainty is associated with the combination of the numerical derivation method with the front position measurement bounded to discrete data. It produces noise in the front velocity signal whose amplitude

is estimated by Eq. (18). The presence of such noise with significant amplitude makes the signal analysis task difficult because the front velocity is not well defined for a given time.

Using Direct Numerical Simulation and Implicit Large Eddy Simulation as data acquisition methods of lock-release density currents, we
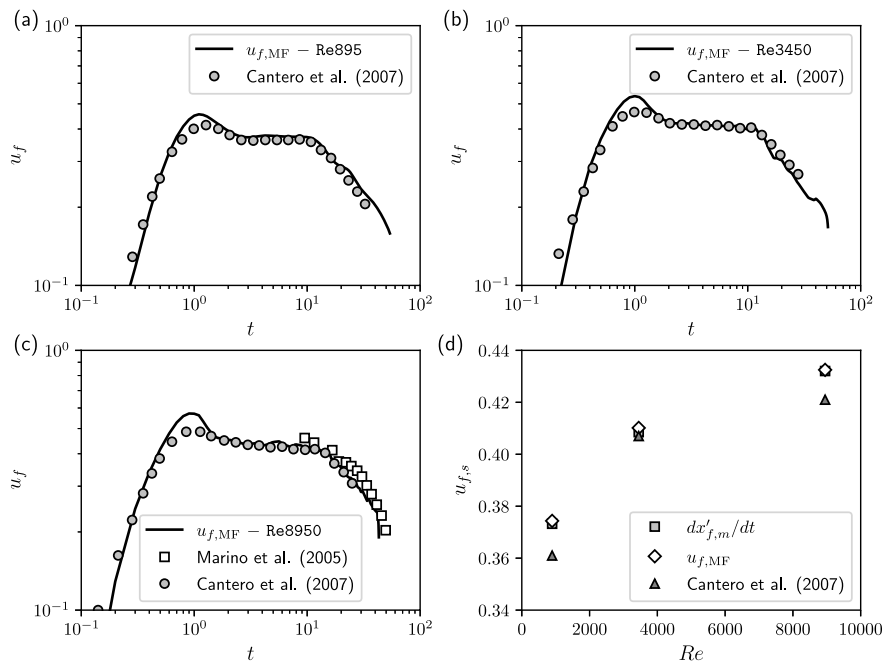
Fig. 10. Front velocity as function of time (a), (b) and (c) and the time-average front velocity during the slumping phase ($u_{f,s}$) as function of the Reynolds number (d). Comparison with results of [4,5] using the moving frame method for the cases Re895 (a), Re3450 (b) and Re8950 (c).

introduced different approaches to measure the flow front position and front velocity. The front position measurement method proposed in this study is based on a local minimum of a momentum quantity. By its robust definition, there is no need to arbitrate a density iso-value, as suggested in previous works. While the front velocity determination method is based on a moving frame approach in which this quantity is evaluated directly from the stream-wise velocity and the scalar fields, the local uncertainty error previously mentioned is not added. The moving frame method results in a smooth front velocity signal, even when the Implicit Large Eddy Simulation approach is considered. It is noteworthy that smoothing data filters were not considered, and all front velocity results are presented in its raw form.

We presented numerical simulations with similar parameters to the "planar small release" series from [5]. When compared with this reference work, our results are mostly in good agreement and present only small deviations of 3.5% in the time average front velocity during the slumping phase for $Re = 895$. In general, the performed simulations reproduce all expected behaviors of lock-release density currents. The proposed front position and front velocity measurement methods can extract data that shows that.

The methods discussed in this work can be easily applicable to numerical simulations datasets, and also from physical experiments when the stream-wise velocity (Eqs. (8) and (22)) and density (Eq. (22)) temporal series are available.

CRediT authorship contribution statement

Bruno Avila Farenzena: Conceptualization, Methodology, Software, Validation, Writing – original draft, Writing – review & editing, Visualization. **Jorge Hugo Silvestrini:** Validation, Resources, Writing – review & editing, Supervision.

Declaration of competing interest

The authors declare that they have no known competing financial interests or personal relationships that could have appeared to influence the work reported in this paper.

Table A.2
Numerical simulations parameters for the mesh convergence tests. All simulations of this table corresponds to planar releases with $L_1 = 8$, $L_{1,b} = 1$, $L_2 = 1$, $L_3 = 1$, $t_f = 20$ and $Sc = 1$.

Simulation	Re	$n_1 \times n_2 \times n_3$	Δt	Approach
Re895mesh1	895	$1025 \times 129 \times 128$	2×10^{-4}	DNS
Re895mesh2	895	$641 \times 81 \times 80$	5×10^{-4}	DNS
Re895mesh3	895	$481 \times 61 \times 60$	10^{-3}	DNS
Re895mesh4	895	$321 \times 41 \times 40$	1.2×10^{-3}	DNS
Re3450mesh1	3450	$2881 \times 361 \times 360$	2×10^{-4}	DNS
Re3450mesh2	3450	$1921 \times 241 \times 240$	2.5×10^{-4}	DNS
Re3450mesh3	3450	$1281 \times 161 \times 160$	5×10^{-4}	DNS
Re3450mesh4	3450	$961 \times 121 \times 120$	10^{-3}	DNS
Re8950mesh1	8950	$1281 \times 161 \times 160$	4×10^{-4}	ILES
Re8950mesh2	8950	$801 \times 101 \times 100$	8×10^{-4}	ILES
Re8950mesh3	8950	$513 \times 65 \times 64$	1.2×10^{-3}	ILES
Re8950mesh4	8950	$401 \times 51 \times 50$	1.2×10^{-3}	ILES

Appendix. Mesh convergence

Preliminary simulations with reduced domain were performed, to choose the best numerical parameters of the main numerical simulations. The time-averaged slumping phase front velocity was measured for each case. Such test simulations consists in the same flow configuration presented previously but with $L_1 = 8$ and $t_f = 20$, which numerical parameters are summarized in Table A.2.

Taking the time-average front velocity during the slumping phase of the finest mesh for each Reynolds number value, we evaluate the relative error, as presented in Fig. A.11. To perform the simulations present in Section 6, we choose the coarser mesh with the relative error
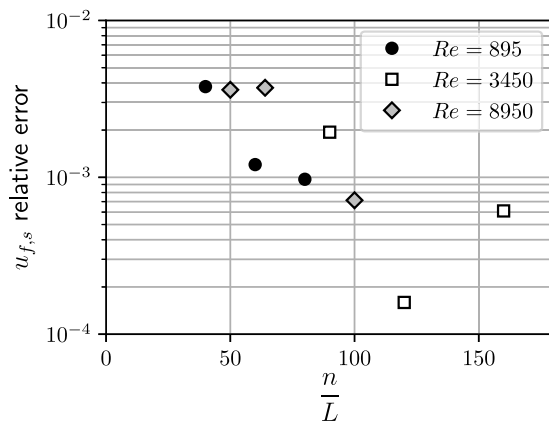
Fig. A.11. Time-averaged front velocity during the slumping phase as function of the grid points density for each test case. Results for $Re = 895$ (a), $Re = 3450$ (b) and $Re = 8950$ (c).

lower than 10^{-3}, which in this case is `Re895mesh2`, `Re3450mesh3` and `Re8950mesh2`.

References

[1] Ungarish M. An introduction to gravity currents and intrusions. CRC Press; 2009.

[2] Simpson J. Gravity currents: In the environment and the laboratory. In the environment and the lab, Cambridge University Press; 1999.

[3] Hacker J, Linden P, Dalziel S. Mixing in lock-release gravity currents. Dyn Atmos Oceans 1996;24(1):183–95. http://dx.doi.org/10.1016/0377-0265(95)00443-2.

[4] Marino BM, Thomas LP, Linden PF. The front condition for gravity currents. J Fluid Mech 2005;536:49–78. http://dx.doi.org/10.1017/S0022112005004933.

[5] Cantero MI, Lee JR, Balanchandar S, García MH. On the front velocity of gravity currents. J Fluid Mech 2007;586:1–39. http://dx.doi.org/10.1017/S0022112007005769.

[6] Fragoso AT, Patterson MD, Wettlaufer JS. Mixing in gravity currents. J Fluid Mech 2013;734:R2. http://dx.doi.org/10.1017/jfm.2013.475.

[7] Espath L, Pinto L, Laizet S, Silvestrini J. Two- and three-dimensional direct numerical simulation of particle-laden gravity currents. Comput Geosci 2014;63:9–16. http://dx.doi.org/10.1016/j.cageo.2013.10.006.

[8] Sher D, Woods AW. Gravity currents: entrainment, stratification and self-similarity. J Fluid Mech 2015;784:130–62. http://dx.doi.org/10.1017/jfm.2015.576.

[9] Pelmard J, Norris S, Friedrich H. LES grid resolution requirements for the modelling of gravity currents. Comput & Fluids 2018;174:256–70. http://dx.doi.org/10.1016/j.compfluid.2018.08.005.

[10] Falco MCD, Ottolenghi L, Adduce C. Dynamics of gravity currents flowing up a slope and implications for entrainment. J Hydraul Eng 2020;146(4):04020011. http://dx.doi.org/10.1061/(ASCE)HY.1943-7900.0001709.

[11] De Falco M, Adduce C, Negretti M, Hopfinger E. On the dynamics of quasi-steady gravity currents flowing up a slope. Adv Water Resour 2021;147:103791. http://dx.doi.org/10.1016/j.advwatres.2020.103791.

[12] Frantz RA, Deskos G, Laizet S, Silvestrini JH. High-fidelity simulations of gravity currents using a high-order finite-difference spectral vanishing viscosity approach. Comput & Fluids 2021;221:104902. http://dx.doi.org/10.1016/j.compfluid.2021.104902.

[13] Huppert HE, Simpson JE. The slumping of gravity currents. J Fluid Mech 1980;99(4):785–99. http://dx.doi.org/10.1017/S0022112080000894.

[14] Zgheib N, Bonometti T, Balachandar S. Direct numerical simulation of cylindrical particle-laden gravity currents. Comput & Fluids 2015;123:23–31. http://dx.doi.org/10.1016/j.compfluid.2015.09.001.

[15] Francisco E, Espath L, Laizet S, Silvestrini J. Reynolds number and settling velocity influence for finite-release particle-laden gravity currents in a basin. Comput Geosci 2018;110:1–9. http://dx.doi.org/10.1016/j.cageo.2017.09.010.

[16] Lombardi V, Adduce C, Rocca ML. Unconfined lock-exchange gravity currents with variable lock width: laboratory experiments and shallow-water simulations. J Hydraul Res 2018;56(3):399–411. http://dx.doi.org/10.1080/00221686.2017.1372817.

[17] Inghilesi R, Adduce C, Lombardi V, Roman F, Armenio V. Axisymmetric three-dimensional gravity currents generated by lock exchange. J Fluid Mech 2018;851:507–44. http://dx.doi.org/10.1017/jfm.2018.500.

[18] Wilson RI, Friedrich H, Stevens C. Flow structure of unconfined turbidity currents interacting with an obstacle. Environ Fluid Mech 2018;18(6):1571–94. http://dx.doi.org/10.1007/s10652-018-9631-7.

[19] Wilson RI, Friedrich H, Stevens C. Quantifying propagation characteristics of unconfined turbidity currents interacting with an obstacle within the slumping regime. J Hydraul Res 2019;57(4):498–516. http://dx.doi.org/10.1080/00221686.2018.1494054.

[20] Hoult DP. Oil spreading on the sea. Annu Rev Fluid Mech 1972;4(1):341–68. http://dx.doi.org/10.1146/annurev.fl.04.010172.002013.

[21] Huppert HE. The propagation of two-dimensional and axisymmetric viscous gravity currents over a rigid horizontal surface. J Fluid Mech 1982;121:43–58. http://dx.doi.org/10.1017/S0022112082001797.

[22] Bartholomew P, Deskos G, Frantz RA, Schuch FN, Lamballais E, Laizet S. Xcompact3D: An open-source framework for solving turbulence problems on a cartesian mesh. SoftwareX 2020;12:100550.

[23] Lele SK. Compact finite difference schemes with spectral-like resolution. J Comput Phys 1992;103(1):16–42.

[24] Kravchenko A, Moin P. On the effect of numerical errors in large eddy simulations of turbulent flows. J Comput Phys 1997;131(2):310–22.

[25] Dairay T, Lamballais E, Laizet S, Vassilicos JC. Numerical dissipation vs. subgrid-scale modelling for large eddy simulation. J Comput Phys 2017;337:252–74.

[26] Ellison TH, Turner JS. Turbulent entrainment in stratified flows. J Fluid Mech 1959;6(3):423–48. http://dx.doi.org/10.1017/S0022112059000738.

[27] Birman VK, Martin JE, Meiburg E. The non-Boussinesq lock-exchange problem. Part 2. High-resolution simulations. J Fluid Mech 2005;537:125–44. http://dx.doi.org/10.1017/S0022112005005033.

[28] Hughes GO, Linden PF. Mixing efficiency in run-down gravity currents. J Fluid Mech 2016;809. http://dx.doi.org/10.1017/jfm.2016.696.

[29] Simpson JE. Effects of the lower boundary on the head of a gravity current. J Fluid Mech 1972;53(4):759–68. http://dx.doi.org/10.1017/S0022112072000461.